Available online at www.sciencedirect.com
SCIENCE DIRECT
International Journal of Heat and Mass Transfer 49 (2006) 3045–3059
International Journal of HEAT and MASS TRANSFER
www.elsevier.com/locate/ijhmt

Heat transfer of impinging jet-array over convex-dimpled surface

Chang Shyy Woei [a,*], Jan Yih Jena [b], Chang Shuen Fei [b]

[a] Thermal Fluids Laboratory, National Kaohsiung Marine University, No. 142, Haijhuan Road, Nanzih District, Kaohsiung City 81143, Taiwan, ROC
[b] Department of Marine Engineering, National Kaohsiung Marine University, No. 142, Haijhuan Road, Nanzih District, Kaohsiung City 81143, Taiwan, ROC

Received 31 August 2005; received in revised form 3 February 2006
Available online 18 April 2006

Abstract

A detailed heat transfer measurement over a convex-dimpled surface of impinging jet-array with three eccentricities (E/H) between jet-centre and dimple-centre is performed. These surface dimples considerably modify heat transfers from smooth-walled scenarios due to different impinging topologies for jet array with modified inter-jet reactions. Heat transfer variations caused by adjusting jet Reynolds number (Re) and separation distance (S/D_j) over the ranges of $5000 \leqslant Re \leqslant 15{,}000$ and $0.5 \leqslant S/D_j \leqslant 11$ with three eccentricities of $E/H = 0$, 1/4 and 1/2 are examined. A selection of experimental data illustrates the isolated and interactive influences of Re, S/D_j and E/H on local and spatially averaged heat transfers. In conformity with the experimentally revealed heat transfer physics, a regression-type analysis is performed to generate a set of heat transfer correlations, which permit the evaluations of spatially averaged Nusselt numbers over central jet region of dimpled impinging surface.

Keywords: Impinging jet-array; Convex-dimpled impinging surface

1. Introduction

Jet impingement heat transfer provides high local heat transfer rate that serves a variety of applications ranging from cooling of gas turbine hot-components to rapid convective heating such as annealing of glass and heat treatment of metals. There have been numerous experimental and theoretical studies investigating heat transfers of impinging jet and jet array [1–37]. There are fundamental differences in the fluid mechanics between single and multiple impinging-jets due to the jet-to-jet interactions prior to and after their impingement on the surface. The factors those influence heat transfers of impinging jet-arrays include turbulence [2], entrainment [3], nozzle geometry [4–6], separation distance [1–6], jet incidence angle [7], surface condition of impinging plate [8–10], wall-jet interaction [11–17], jet spacing [18] and external factors such as the crossflow [19–23], spent flow condition [24,25], drainage [26,12] and jet pulsation [27]. The impacts of these factors on heat transfer are generally described as functions of separation distance and jet Reynolds number for a set of geometrical specifications. A major disadvantage of impinging jet-array is that the spatial heat transfer variations over impinging surface could be highly non-uniform. Therefore, the flow and geometrical parameters of a multiple-jet system have to be carefully selected in order to provide the required heat transfer rates with acceptable uniformity over the impinging surface.

Lee and Vafai [28] developed a procedure to determine the optimal separation distance and nozzle-to-nozzle spacing for an impinging jet-array using the previous experimental results [3,11,21,23,29]. The maximum convective capability of an impinging jet-array is significantly affected by the manner of treating the spent flow [28]. The spent fluid in the wall-jet region is forced to flow laterally over the impinging surface. The networks along which the radial

* Corresponding author. Tel.: +886 7 810 0888/5216; fax: +886 7 572 1035.
E-mail address: swchang@mail.nkmu.edu.tw (S.W. Chang).

0017-9310/$ - see front matter © 2006 Elsevier Ltd. All rights reserved.
doi:10.1016/j.ijheatmasstransfer.2006.02.030

Nomenclature

A, B	coefficients
D_j	diameter of jet nozzle for baseline array (m)
E	eccentricity between jet-centre and dimple-centre (m)
k_f	thermal conductivity of fluid (W/m K)
H	jet-to-jet space (m)
$\dot{M}$	total mass flow rate issued from jet array
Nu	local Nusselt number $= qD_j/k_f(T_w - T_j)$
$\overline{Nu}_C$	area-averaged Nusselt number of central jet region
q	convective heat flux (W/m^2)
Re	Reynolds number $= \frac{4}{12\pi}\frac{\dot{M}}{D_j\mu}$
S	separation distance (m)
T_j	fluid temperature at exit of nozzle (°C)
T_f	film temperature $= (T_w + T_j)/2$ (°C)
T_w	wall temperature (°C)
X, Y	dimensionless location $(x/D_j, y/D_j)$

Greek symbols

μ	fluid dynamic viscosity (kg/ms)
ρ	fluid density (kg/m^3)

spent fluid is convected generate the hexagonal and square webs on the impinging surface for the staggered and in-line jet arrays, respectively [14,15]. The development of such radial network is a result of jet-to-jet interaction after impingement. With certain flow conditions, the secondary heat/mass transfer maximum could develop in the interaction zone [13,14,18,24,30,31]. A ring of secondary stagnation-heat-transfer contour that surrounds the central confined jet could appear when jet Reynolds number and separation distance are, respectively, large and small [14]. The secondary stagnation heat transfer level decreases with the increases of nozzle-to-nozzle spacing [13] and separation distance [14]. This result typifies the influence of boundary layer transition on heat transfer owing to the radial flow acceleration and deceleration.

When the impinging jet-array is confined, the exit stream of the spent fluid could generate the crossflow that deflects or diffuses the jet momentum. In general, local heat transfers over the impinging surface are deteriorated by the crossflow but could be enhanced when the separation distance is very small [19,20,23,28]. The crossflow effect is minimized by locating the spent air exits through the openings in the impinging surface or in the nozzle plate [18,24,12]. The other measure to assist the transportation of radial spent fluid is to use the grooved orifice plate to eject the multiple jets. The considerable heat transfer enhancement over the most confined central jet region in a jet array is attainable by ejecting jets from the grooved surface [6]. This particular measure not only provides favourable treatment of spent fluids but the deflected jets confined in the groove could also enrich the central jet momentum via the enhanced entrainment at small separation distance.

Most of the previous studies have being concerned with either single-jet or jet array impinging on flat surface. Only a few of recent studies concerns more complex geometries of impinging surfaces. These impinging surfaces resemble those of electronic component and pin-fin array [32,33], cylindrical food product [10] and rib-roughened surfaces [34–36]. For an axisymmetric jet impinging on a heated pedestal [32], the jet-flow develops into a free jet after leaving the nozzle and decelerates as it impinges on top of the pedestal. A very thin boundary layer approaches the sharp corner of pedestal, where separation occurs. A highly turbulent region develops along the separated shear layer, then reattaches to the base plate. The recirculation zone that forms at the side of pedestal under the separated shear layer becomes the thermal barrier. Under the recirculation zone, heat transfers reach local minimum on the bottom corner of pedestal that gradually increase along the base plate. A local maximum base-plate heat transfer point is positioned at the location slightly upstream of the reattachment point. When the single pedestal is extended to the repeated rectangular ribs [34], the wall-jet stream could be trapped into the cavity between neighbouring ribs that reduces local heat transfer. At the spacing between neighbouring rectangular ribs close to the stagnation point, the air bobble that encloses the cavity prevents penetration of impinging jet into the cavity and the recirculation zone. This effect also impairs local heat transfers on and around the stagnation point. Nevertheless, by replacing the rectangular ribs with triangular ribs that provides a widely opened spacing between neighbouring ribs [35], the impinging or the wall jet is more readily to penetrate into the cavity and impinge on the wall. Impingement heat transfers along the triangular ribbed surface are higher than those counterparts along the rectangular ribbed wall. With a jet-flow impinging on a circular cylinder, the flow accelerates beyond the stagnation point that follows the curvature of cylinder up to the separation point, where the flow yields to a wall jet [10]. Below the separated shear layer, the flow is reversed that forms a wake, which creates an increase in velocity and heat transfer. For cooling or heating of a large area, the elements of surface roughness such as the pedestal and the rectangular, triangular and circular protrusions are repeated and the jet array configuration have to be used. In this study, the impinging surface has convex dimples arranged as the in-lined array. These convex dimples could affect the jet-flow structures [10] with weakened jet-to-jet interference and promote the turbulent mixing by introducing the separation shear layers [10,32]. It is expected that heat transfer enhancement with improved uniformity could

be achieved by impinging the jet array over convex dimpled target surface. None of the aforementioned works have studied this heat transfer configuration.

The present study performs the detailed heat transfer measurements of an impinging jet-array over the convex-dimpled surface. Three test conditions are performed to unravel the different heat transfer patterns caused by varying the distance between jet-centre and dimple-centre. The reference condition is referred to as the inline configuration. When the jet-centres are inline with the dimple-centres, the jets impinge directly onto the apexes of convex dimples. The remaining two test series allow the jet array to be shifted horizontally with distances of 1/4 and 1/2 jet-to-jet spacing. The shifting length is referred to as the eccentricity between the jet-centre and dimple-centre. The detailed distributions of local Nusselt number contours and spatially averaged heat transfer data, evaluated from the infrared thermal images of the impinging dimpled surfaces, are presented over a range of separation distances and Reynolds numbers for three test configurations. An additional series of tests using the smooth-walled impinging surface are performed to generate the heat transfer references for comparing the heat transfer results acquired from the dimpled surface. The impacts of convex dimples and eccentricity on heat transfer are subsequently analyzed to assist the derivation of empirical heat transfer correlations.

2. Experimental details

2.1. Apparatus

The experimental apparatus is shown in Fig. 1. Prior to entering the 200 mm long, 15 mm wide square-sectioned

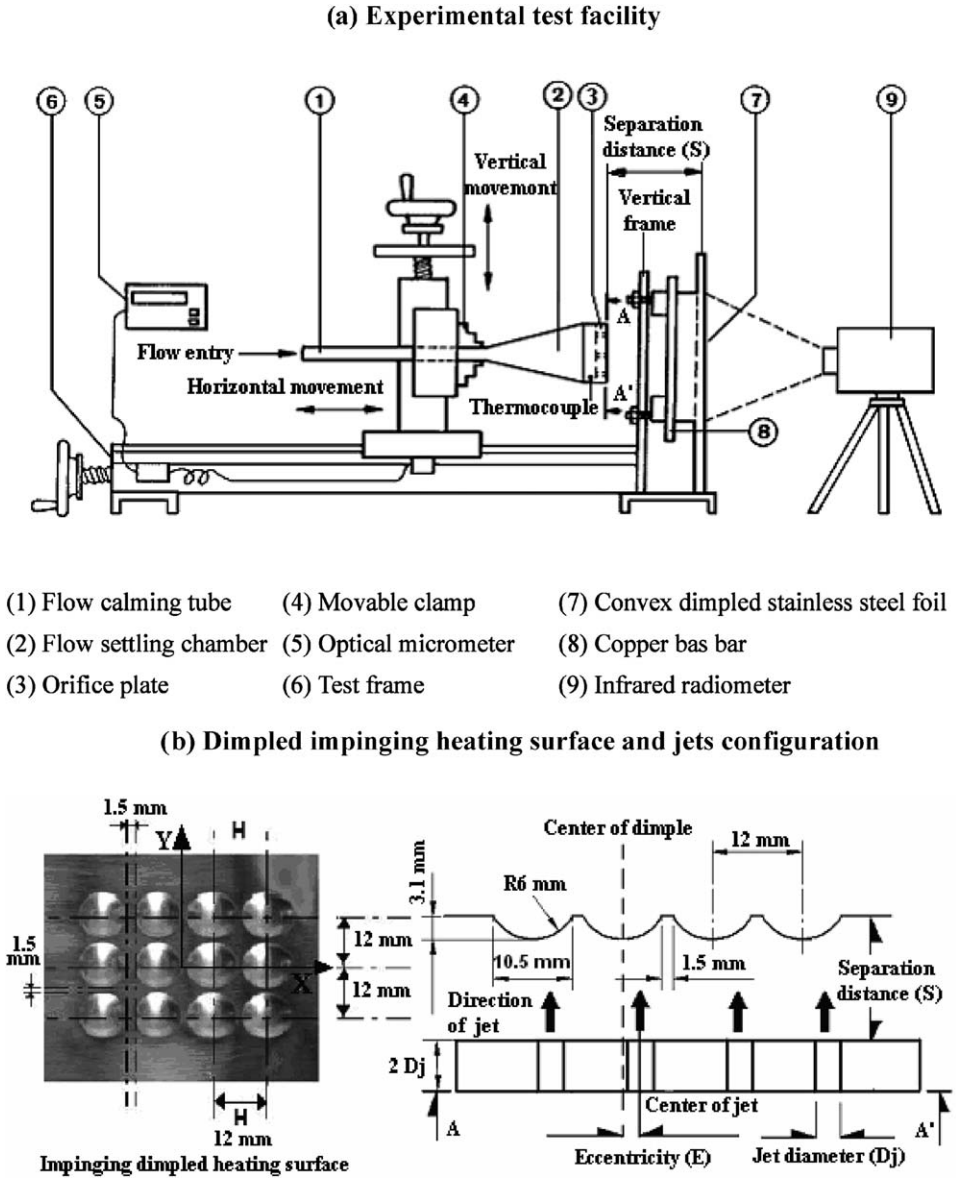

Fig. 1. Experimental apparatus.

flow-calming-tube (1), the air fed form the IWATA SC 175C screw-type compressor unit was dehumidified and cooled to the ambient temperature through a refrigerating unit that was integrated with the compressor. The dry and cooled airflow was then guided through a set of pressure regulator and filter with the flow rate to be metered and adjusted by a Tokyo Keiso TF-1120 mass flow meter and a needle valve, respectively. The adjusted and metered test fluid was then directed into the flow-settling chamber (2). The divergent flow settling chamber is of 120 mm long with the orifice plate (3) fitted at the wide end. A 3×4 array of jets was issued from the nozzles through the orifice plate. Twelve in-line jet-nozzles were equally spaced over the orifice plate with the jet diameter (D_j) of 3 mm. The jet-diameter was selected as the characteristic length for defining the Reynolds and Nusselt numbers. As indicated in Fig. 1b, the thickness of orifice plate was two jet diameters. Each nozzle had abrupt inlet and exit. The dimensionless jet-to-jet spacing, H/D_j, was 4. The complete jet array assembly was fixed and centred on a movable clamp (4). The vertical and horizontal movements of this clamp were adjusted by two independent thread mechanisms, which could be precisely adjusted in order to position the jet array at the predefined location. The separation distance between the outer-face of orifice plate and the flat-edge of convex-dimpled surface, as indicated in Fig. 1b, could be precisely controlled. An optical micrometer (5) with the precision of 0.01 mm was mounted on the test frame (6) to measure the separation distance. The jets issued from the orifice plate impinged horizontally against a very thin (0.1 mm) and 65 mm wide stainless-steel target foil (7). Twelve equal-spaced convex dimples with the identical pitch as that of jet-nozzles were forged from a continuous thin stainless steel foil. The photograph of dimpled heating foil and the detailed geometrical specifications for this convex-dimpled impinging surface were depicted in Fig. 1b. The check of the dimpled stainless foil indicated that the maximum non-uniformity in thickness was less than 1% so that the electrical resistance of the steel foil was approximately uniform. The coordinate system adopted by the present study was indicated on the impinging surface as shown in Fig. 1b that the origin was specified at the centre of dimple-array. This convex dimpled stainless steel foil was stretched tightly between two copper bus bars (8) on the test facility. As indicated in Fig. 1a, these two copper bus bars (8) were attached with the vertical frames by threads which provided the required stretching force to tighten the heating foil fixed on the copper bus bars (8). To perform the tests involving eccentricity between jet-centre and dimple-centre, the heating foil was horizontally shifted. For all the test conditions, the foil deflection under the maximum Reynolds number tested at the smallest separation distance was less than 0.02 mm as measured by a precision calipers. The adjustable high current DC electrical power was directly fed into the thin steel foil to generate the basically uniform heat flux surface. The temperatures of the heating surface under each test condition were imaged by a two-dimensional NEC TH3101-MR infrared radiometer (9). For this thermal image processing system, it took 0.3 s to complete a full-field of 239×255 matrix scan. The back surface of the heating foil was painted black in order to minimize the background reflection and to increase the emission.

2.2. Program and procedures

The experimental program involved two phases. Initially the effect of convex dimples on heat transfer was checked out with a series of baseline tests without eccentricity over a range of separation distances and Reynolds numbers. The results acquired from this series of tests were compared with the data obtained from the smooth-walled impinging surface. This was followed by a similar series of experiments for test conditions with eccentricities of 1/4 and 1/2H. With the same ranges of flow and geometric parameters, the heat transfer results from the two phases were compared to reveal the heat transfer modifications caused by the different eccentricities between the jet-centre and dimple-centre. Finally, the empirical correlations for the spatially averaged heat transfer rates over the central region of dimpled surface for three sets of test scenarios were derived as the strategic aim of the present study.

For each individual test, the apparatus was allowed to achieve steady state. A steady state was assured when several successive scans of wall temperatures over the impinging surface were less than 0.3 °C for each test at the predefined flow rate and heating power. The percentage of 0.3 °C was in the range of 0.18–0.9% of the wall temperatures tested. To account for the viscous heating effect over the dimpled impinging surface, the reference fluid temperature adopted to define the local Nusselt number was initially selected as the adiabatic wall temperature. Over the entire tested conditions performed by the present study, the maximum differences between the adiabatic wall temperature and jet temperature were less than 0.1 °C which was 0.67% in percentage. Thus, the reference fluid temperature for defining local heat transfer rate was replaced by jet temperature. The jet temperature, T_j, was measured using a thermocouple penetrated into the plenum chamber as indicated in Fig. 1. The effect of variable properties was embodied in the film temperature, T_f, defined as $T_f = (T_w + T_j)/2$. All the fluid properties were evaluated based on the local film temperature. With tests at each $Re - S/D_j$ options, the heater power was fixed at 460 W that provided the supplied heat flux of 4641.78 W/m^2. The electrical heating power was measured by the wattage meter. The area used to define the total heat flux included the surface areas of convex dimples. This heating power resulted in the wall-to-jet temperature differences in the range of 7–54 °C. Along with the measured heating power and jet temperature, T_j, the local Nusselt number distributions at the prescribed Reynolds number and separation distance were evaluated. The local Nusselt number is evaluated as

$$Nu = qD_j/k_f(T_w - T_j). \quad (1)$$

In Eq. (1), the convective heat flux, q, was calculated from the electrical dissipation measured over the entire heating surface with the heat loss to be subtracted. The characteristics of external heat loss at different heating levels were determined through a number of heat loss calibration runs. For each set of calibration runs, the flow was blocked off and the impinging surface was fitted with thermal insulation. Under such circumstance, the heat supplied to the heating foil was entirely lost into atmosphere from the back of the impinging surface and balanced with the amount of heat loss at the corresponding steady-state temperature distribution. A review of the temperature data collected from the heat-loss calibration test runs showed less than 2.95% of non-uniformity in the wall temperature distributions. Thus, by plotting the heat flux applied for each heat-loss calibration test against the corresponding steady wall-to-ambient temperature difference reveals the proportionality between the heat loss flux and the prevailing wall-to-ambient temperature difference. This proportionality was incorporated into the data processing program to evaluate the local heat-loss flux. The maximum local heat loss flux was divided by the total heat flux supplied to define the maximum percentage of the heat loss. The maximum heat loss flux for the entire sets of data generated was 9.6% of the total heat flux supplied. It is worth noting that, when the jet array is issued from the orifice plate, the pressure distribution over the impinging surface varies with the flow and geometric parameters such as Reynolds number, separation distance and the dimpled surface. As a result, the rate of mass flow through each nozzle in the orifice plate is different and is functionally related with Re, S/D_j and geometric features of the impinging surface [25]. The adjustment of Reynolds number or the geometric parameters of the jet-array system provide a unique mass flux distribution for the jets issued from the orifice plate. The different mass flow rate through each nozzle in an array issued from the orifice plate reflects the realistic flow phenomena when the jet arrays are issued from an orifice plate during the engineering application, which effect on heat-transfer was also an engineering focus for investigation [24,25,12]. The Reynolds number is specified as $4\dot{M}/12\pi D_j\mu$, where $\dot{M}$ is the total mass-flow-rate fed to the 12 jets. The range of Reynolds numbers tested ensured the turbulent jets were examined because the jet became turbulent with $Re \geqslant 3000$ [37]. The Reynolds numbers tested were 5000, 7500, 10,000, 12,500 and 15,000. For each tested Reynolds number, heat transfer coefficients with eleven separation distances of 0.5, 1.5, 2, 3, 4, 5, 6, 7, 8, 10 and 11 D_j were measured.

The experimental repeatability of temperature measurement using NEC TH3101-MR infrared radiometer was previously carried out [6]. The maximum uncertainty of temperature measurement was in the range of ± 0.7 °C for the present system. This uncertainty of temperature measurement was the major source to attribute the uncertainties for the coolant's thermal conductivity, fluid density and viscosity. Following the policy of ASME on reporting the uncertainties in experimental measurements and results [38], the maximum uncertainty associated with the local Nusselt and Reynolds numbers were estimated to be 9.7% and 6.5%, respectively.

3. Results and discussion

3.1. General results

To highlight the impact of surface dimples on heat transfer, a set of comparable results obtained from the smooth-walled and convex-dimpled impinging surfaces are depicted in Fig. 2. Fig. 2a and b shows the distributions of Nusselt number contour over smooth-walled and convex-dimpled surfaces with $Re = 7500$ and $S/D_j = 4$. The boundaries of central-unit-cell and convex-dimple are specified in Fig. 2. The spatially averaged Nusselt numbers over the entire scanned area and the central-unit-cell are evaluated as $\overline{Nu}$ and $\overline{Nu}_C$, respectively. The values of $\overline{Nu}$ and $\overline{Nu}_C$ are, respectively, obtained by averaging the local Nusselt numbers over the regions of entire scanned area and the central-unit-cell. The interval between two adjacent Nu contours in Fig. 2a and b remains identical. As shown in Fig. 2a, the Nusselt number contours over the smooth-walled surface distribute symmetrically about X and Y axes. This observation reveals the free surface like jet-flow in the central jet region at separation distance of $4D_j$. The distributing pattern of Nu contours depicted in Fig. 2a follows the typical result of impinging jet-array with the maximum heat transfer rate at each stagnation point. Nine heat transfer humps centred at the stagnation points feature the impacts of impinging jets on heat transfer augmentation. In contrast to these improving heat transfer humps, there are regions of concave Nu surfaces developed at the inter-jet regions as shown in Fig. 2a. The locally minimum Nusselt numbers in these regions generally take place at the geometric centres of four surrounding jets that are the intersections of flow paths along which the radial spent fluids are convected. This type of heat transfer impediment reflects the influences of weakened wall-jet flow momentum and thickened boundary layers due to the collision of radial spreading flows, which is referred to as the jet-to-jet interference. The moderation of jet-to-jet interferences and/or the shrinkage of inter-jet regions could further elevate the values of $\overline{Nu}$ and $\overline{Nu}_C$ for an impinging jet-array system. A cross-examination of distributing patterns of Nu contours for the two scenarios depicted in Fig. 2a and b highlights the shrinkage of inter-jet regions and the elevations of stagnant and spatially averaged Nusselt numbers over the convex-dimpled surface. The concentric Nu contours, centred at the dimple-centre that corresponds to the stagnation point when the eccentricity is zero, develop over each spherical surface-dimple. Nusselt number contours over these convex dimples are much dense than those counterparts over the smooth-walled surface. This is attributed

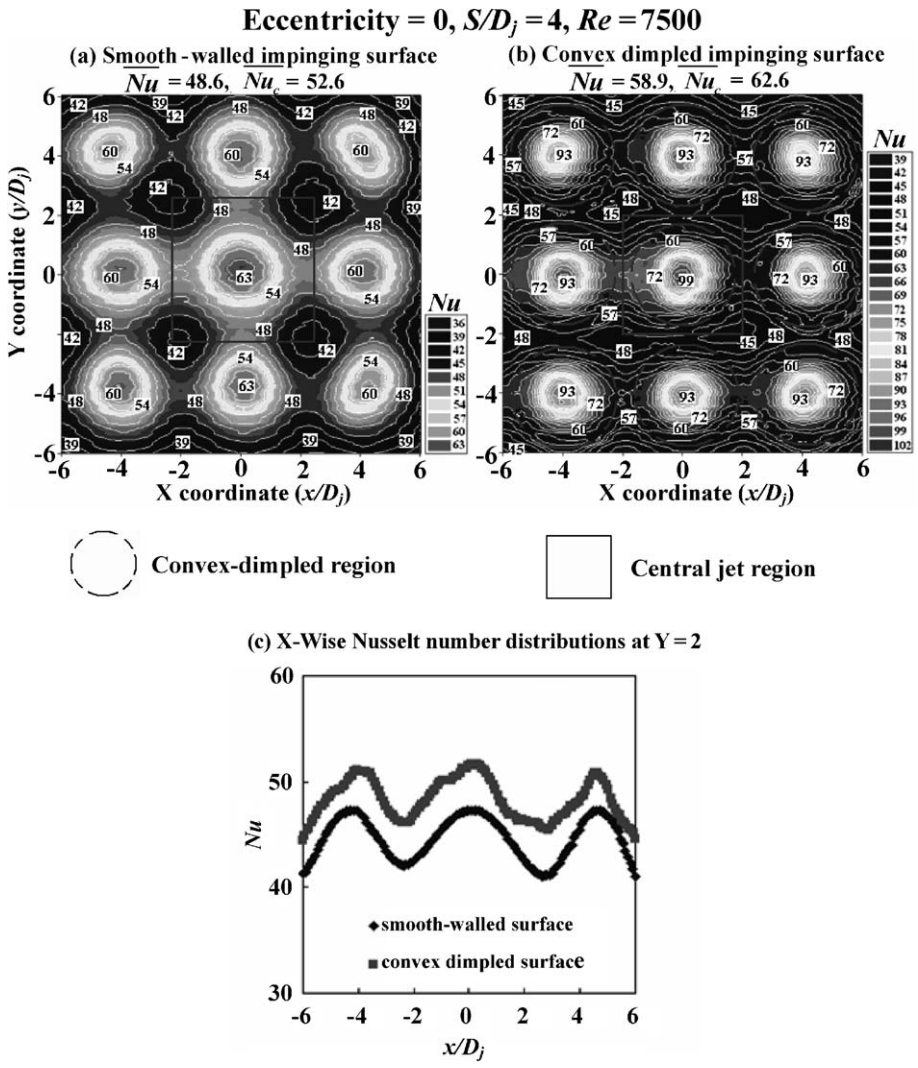

Fig. 2. Typical heat transfer distributions over smooth-walled and convex-dimpled surfaces.

to the considerable elevation of stagnant Nusselt number over each dimple. As indicated in Fig. 2a and b, the stagnant Nusselt number over the convex-dimpled surface reaches almost twofold stagnant *Nu* value over the smooth-walled surface for this set of test condition. These convex dimples also provide considerable heat-transfer impacts over the inter-jet regions. To further probe into this respect, the *X*-wise Nusselt number distributions over the smooth-walled and convex-dimpled surfaces along the horizontal axis of $Y = 2$ are compared in Fig. 2c. The horizontal axis of $Y = 2$ traverses the inter-jet region. As shown in Fig. 2c, the locally minimum heat transfer spots develop at $X = \pm 6$ and ± 2 that correspond to the intersections of radial flow paths for spent fluids. The degree of heat transfer reduction due to jet-to-jet interference in the inter-jet region over the dimpled surface is moderated from the smooth-walled scenario. The convex-dimpled surface for this particular set of test conditions is in favour of moderating jet-to-jet interference and reducing inter-jet regions. This impact on heat transfer for jet array could assist to improve the uniformity of heat transfer distributions over the impinging surface provided the combination of *Re* and S/D_j is adequately selected. In this regard, further increase of Reynolds number and/or decrease of separation distance could alter the beneficial heat transfer impacts attributed from the surface dimples, which will be addressed in the latter sections.

3.2. *Re*, S/D_j and *E*/*H* impacts on heat transfer

The *Nu* distributions over smooth-walled and convex-dimpled surfaces are both symmetrical about *X* and *Y* axes as demonstrated in Fig. 2. This symmetry allows one half of each *Nu* plot typified in Fig. 2 to be representative for the heat transfer scenario detected from any set of test conditions. In order to highlight the impacts of convex-dimpled surface on heat transfer, local Nusselt numbers over dimpled surface are normalized by *Nu* values detected from the smooth-walled surface with identical *X* and *Y* coordinates. The Nusselt number ratio in terms of $Nu/Nu_{\text{smooth-wall}}$ quantifies the local heat transfer variation from the smooth-walled level. Fig. 3 compares the distributions of *Nu* and

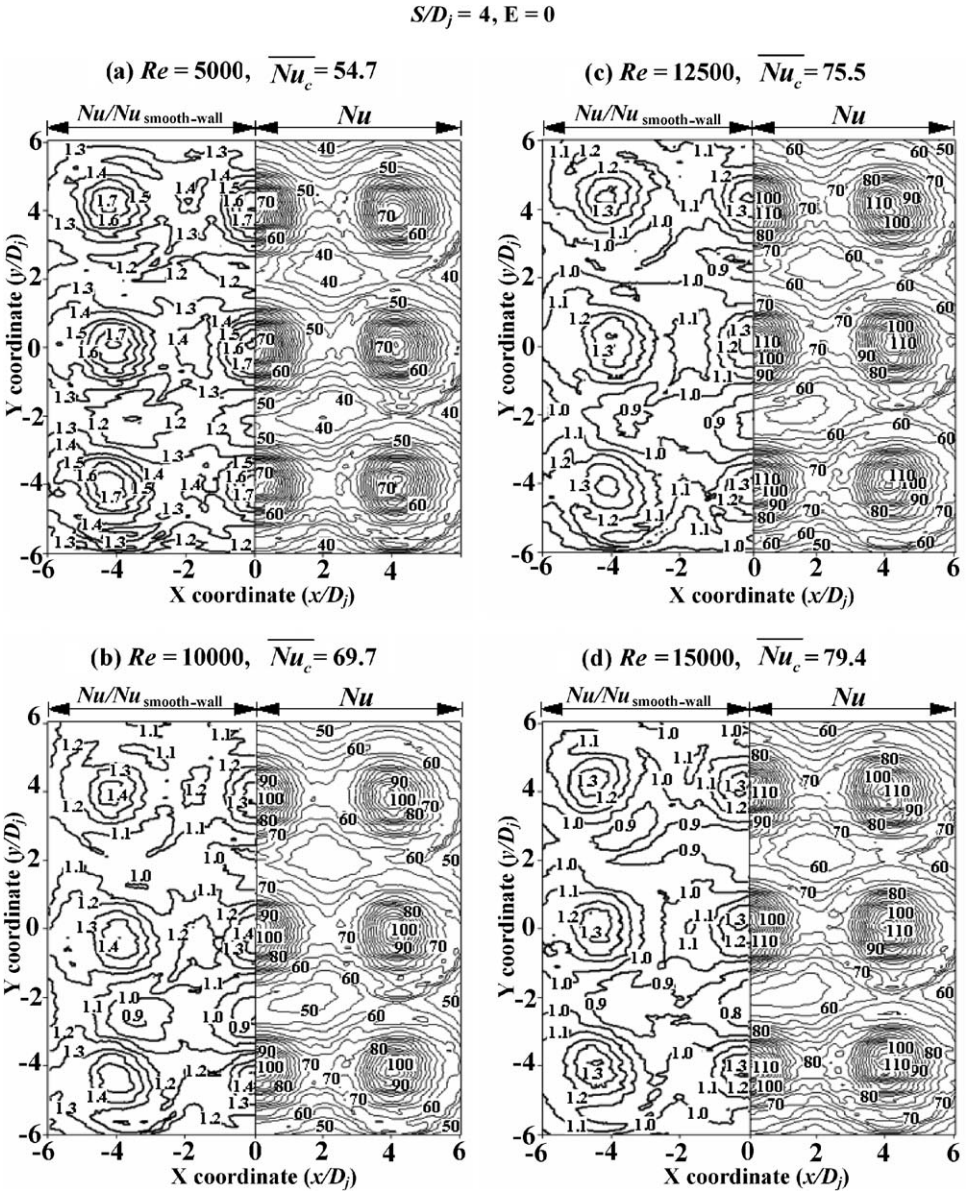

Fig. 3. Effect of jet Reynolds number on heat transfer distributions over convex-dimpled surface with separation distance of $4D_j$.

$Nu/Nu_{\text{smooth-wall}}$ over the dimpled surface for Reynolds numbers of 5000, 10,000, 12,500 and 15,000 at separation distance of $4D_j$ without eccentricity. Each individual plot in Fig. 3 is constructed by the contours of Nu and $Nu/Nu_{\text{smooth-wall}}$ over the respective regions of $0 \leqslant X \leqslant 6$ and $-6 \leqslant X \leqslant 0$. As shown in Fig. 3, the increase of Reynolds number systematically elevates the stagnation heat transfer and $\overline{Nu}_C$ without varying the distributing pattern of Nu contours. Local Nusselt numbers over the hump regions and the inter-jet regions, as shown in Fig. 3, are both elevated when Re increases. But the ratios of $Nu/Nu_{\text{smooth-wall}}$ over the dimpled surfaces are systematically reduced as Re increases. This data trend unravels that the heat transfer augmentation generated by these surface dimples is reduced as Re increases. Heat transfer augmentation also appears to be spatially dependent. As indicated in each plot of Fig. 3, the higher ratios of $Nu/Nu_{\text{smooth-wall}}$ consistently develop over the hump regions in comparison with those in the inter-jet regions. For the test conditions of $S/D_j = 4$ and $Re \leqslant 10{,}000$, Fig. 3a and b shows that the most of $Nu/Nu_{\text{smooth-wall}}$ ratios are above than unity over the dimpled surfaces. Further increase of Reynolds number to 12,500, the ratios of $Nu/Nu_{\text{smooth-wall}}$ start to be less than unity from the inter-jet region, although the heat transfers are still higher than those of smooth-walled counterparts in the hump regions (see Fig. 3c). At Reynolds number of 15,000 as revealed in Fig. 3d, the areas appearing $Nu/Nu_{\text{smooth-wall}} < 1$ are expanded from the inter-jet regions toward the hump regions. The growing rate of inter-jet impacts on heat transfer impediments via increasing Re for convex-dimpled surface appears to be faster than that for the smooth-walled surface. In this respect, the decrease

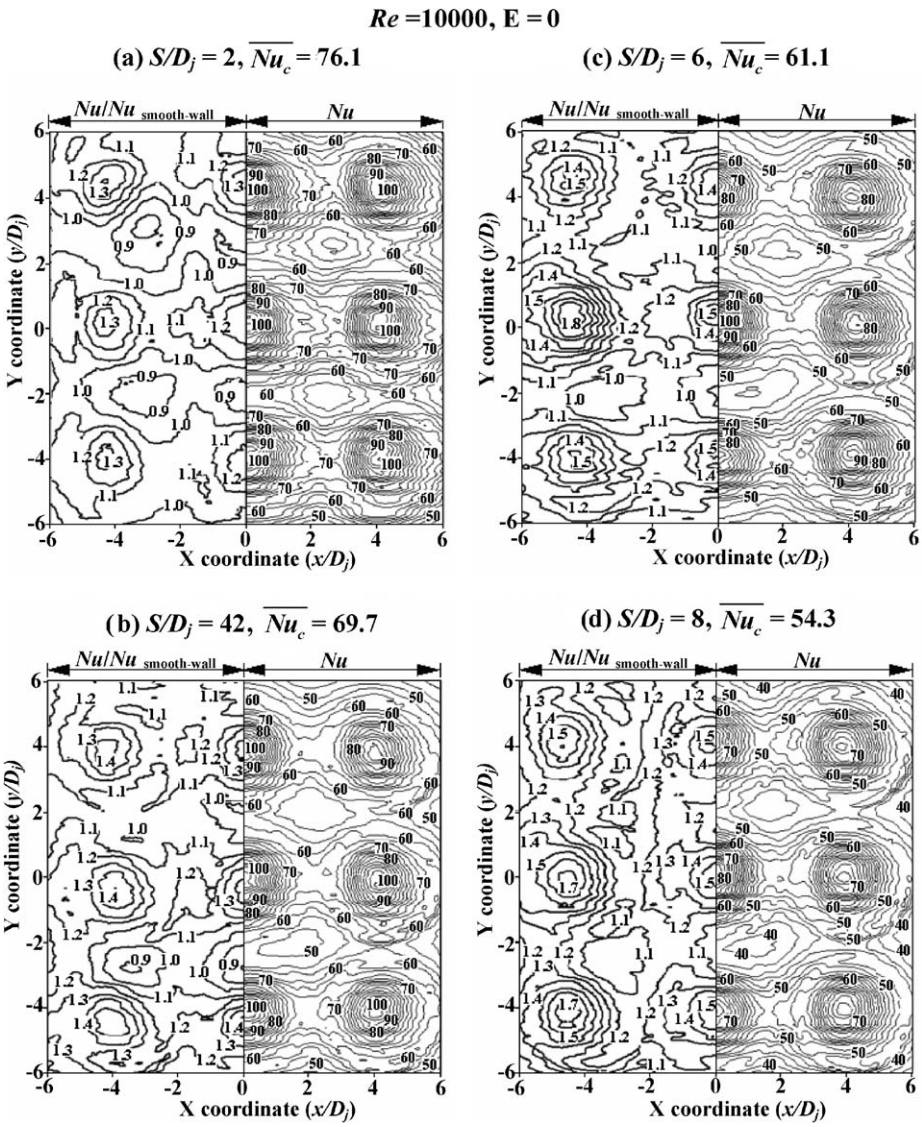

Fig. 4. Effect of separation distance on heat transfer distributions over convex-dimpled surface with jet Reynolds number of 10,000.

(increase) of separation distance could accelerate (decelerate) the impeding impacts of jet-to-jet interferences on local heat transfer over the convex-dimpled surface when eccentricity is zero. Fig. 4 is constructed in the manner to clarify this particular heat transfer physic.

Fig. 4 compares the distributions of Nu and $Nu/Nu_{\text{smooth-wall}}$ over the convex-dimpled surface at separation distances of 2, 4, 6 and 8 S/D_j for Reynolds number of 10,000. In view of the Nu plots shown in Fig. 4a–d, the distributing pattern of Nu contour remains unaltered but the $\overline{Nu}_C$ values are systematically reduced when S/D_j increases. The distributing contours of $Nu/Nu_{\text{smooth-wall}}$ shown in Fig. 4 indicate a trend of increasing $Nu/Nu_{\text{smooth-wall}}$ ratios as S/D_j increases. The plots of $Nu/Nu_{\text{smooth-wall}}$ contours shown from Fig. 4a–d demonstrate the recovery of $Nu/Nu_{\text{smooth-wall}}$ ratios in the inter-jet regions from impediments at $S/D_j = 1.5$ to enhancements at $S/D_j \geqslant 6$. The recovery of $Nu/Nu_{\text{smooth-wall}}$ ratios in the inter-jet region from heat transfer impediment to enhancement as seen in Fig. 4a–d indicates that the jet-to-jet interferences are weakened at a faster rate over the dimpled surface relative to the smooth-walled counterpart as S/D_j increases. This physic could lead to the extension of Re ranges within which the $\overline{Nu}_C$ values over dimpled surface are higher than those over smooth-walled surface as S/D_j increases. A detailed description in this respect will be discussed when the variations of $\overline{Nu}_C$ against Re with different eccentricities are examined.

To highlight the influences of eccentricity between jet-centre and dimple-centre on heat transfer, the distributions of Nu contour at eccentricity ratios (E/H) of 0, 1/4 and 1/2 are compared in Fig. 5 using three sets of test results with different Re and S/D_j. The comparative results between the plots collected in the first and second columns of Fig. 5 indicate the impacts of eccentricity ratio on heat transfer with different Re at a fixed S/D_j of 1.5. When the second and third columns of Fig. 5 are compared, the different Nu profiles attributed from the E/H impacts are revealed

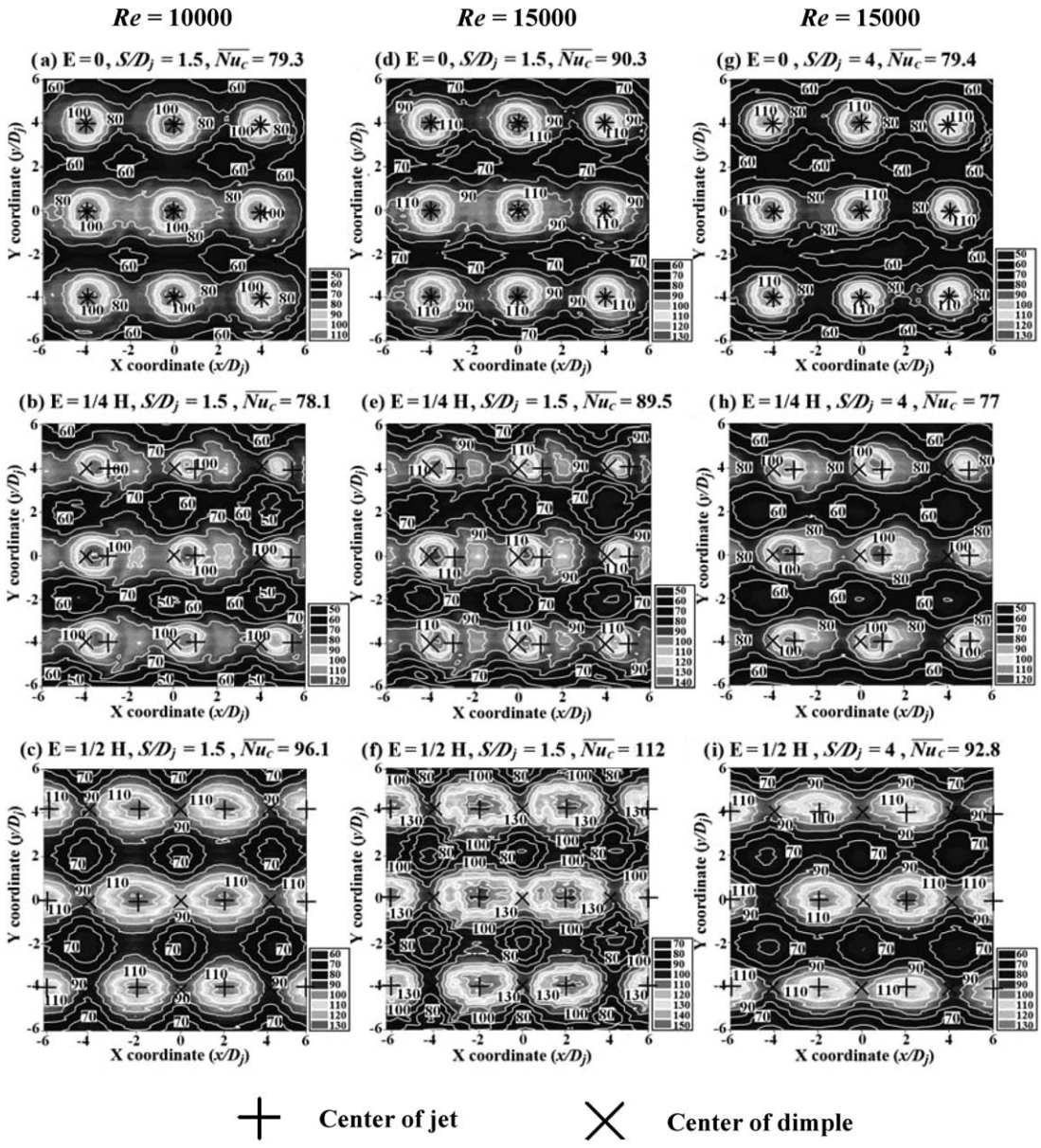

Fig. 5. Effect of eccentricity on heat transfer distribution over convex-dimpled surface with separation of 1.5 and 4 at jet Reynolds number of 10,000 and 15,000.

with different S/D_j at a fixed Re. As a general impact of dimples on Nu distribution, the oval-shaped Nu contours, which are stretched in the horizontal direction from the concentric circular shapes over the smooth-walled surface, are observed for test conditions of $E/H = 0$, 1/4 and 1/2. With test conditions of $E/H = 1/4$ and 1/2, the locations on impinging surface corresponding to the jet-centre and dimple-centre, which are, respectively, indicated as + and × in Fig. 5, are not overlapping. As shown in Fig. 5, the distributing patterns of Nu contour are considerably modified when eccentricity ratio varies. It is worth to note that the topology remains symmetrical about each spot corresponding to jet-centre for test conditions of $E/H = 0$ and 1/2 but is asymmetrical for test conditions of $E/H = 1/4$. As a result, the local Nu peaks that correspond to the stagnation points are consistently developed at jet-centres for all the test scenarios with $E/H = 0$ and 1/2. However, for the test results with $E/H = 1/4$ as demonstrated in Fig. 5b, e and h, the stagnation heat transfers are not resolved at the jet-centres but at the locations between the jet-centre and dimple-centre. This finding indicates that the jet issued from orifice plate is bend toward the dimple-centre by asymmetrical pressure field developed over the dimpled surface when the topology becomes asymmetrical about the jet-centre for test conditions of $E/H = 1/4$. With $E/H = 1/4$, the concave Nu profiles attributed from the jet-to-jet interferences still occupy a considerable portion of impinging surface but are off-centred from the counterparts obtained with $E = 0$. Instead of having the local minimum Nu spot developed at the geometric centre between four surrounding

stagnation points as shown in the test results of $E/H = 0$ and 1/2, the minimum Nu spot in each region with concave Nu profiles is horizontally shifted in the right direction as indicated in Fig. 5b, e and h. The shift of minimum Nu spot indicates the unbalance of radial momentum from four surrounding stagnation points as the jointed consequences of bent-jet and asymmetrical spherical topology. Nevertheless, $\overline{Nu}_C$ values for each comparing pairs of $E = 0$ and $E = 1/4$ are in the close agreements. Further increase of E/H ratio from 1/4 to 1/2, the topology surrounding the stagnation point becomes symmetrical that resolves into another form of symmetrical Nu profiles as demonstrated in Fig. 5c, f and i. Once again, each stagnation point coincides with the jet-centre at the middle position between two dimple-centres. The minimum Nu spot among each inter-jet region for the test results with $E/H = 1/2$ also develops at the geometric centre between four surrounding stagnation points. A comparison of the Nu plots between the test results of $E/H = 0$ and 1/2 unravels that the areas occupied by heat transfer humps are considerably extended for the scenarios with $E/H = 1/2$, which effect has led to the considerable increase of $\overline{Nu}_C$ from the result obtained with $E/H = 0$.

To examine E/H impacts on heat transfer with the comparative manner, a set of selective Nu profiles along $Y = 0$ axis and along three X axes corresponding to the vertical axis that connects three jet-centres for four test scenarios are, respectively, compared in Fig. 6a and b. The locations of jet-centres are marked in Fig. 6a so that the off-set of stagnation point from the jet-centre for test conditions of $E/H = 1/4$ is highlighted. As seen in Fig. 6a, the smooth-walled Nu profiles follow the typical results of impinging jet-array with Nu peak developed at the stagnation point that corresponds to the jet-centre. The locally minimum Nu values develop at the locations of $X = \pm 2$ and ± 6 for smooth-walled case due to jet-to-jet interferences. In view of the Nu profiles over dimpled surface with $E/H = 0$, the locations of Nu peak and local Nu minimum are identical with the smooth-walled counterparts. The Nu values in the inter-jet regions for smooth-walled and $E/H = 0$ conditions are in the similar levels; but the stagnation heat transfer over the dimpled surface with $E/H = 0$ is consistently higher than the smooth-walled level as shown in Fig. 6a. Nevertheless, the increase of Re at fixed S/D_j or decrease of S/D_j at fixed Re could moderate such heat transfer augmentation at the stagnation point over the dimpled surface. It is worth noting that, for the test conditions of $Re \geqslant 10{,}000$ and $S/D_j = 1.5$, heat transfer rates in the inter-jet regions over dimpled surface with $E/H = 0$ and 1/4 are reduced to be less than the smooth-walled levels. These typical heat transfer results for these particular test conditions ($Re \geqslant 10{,}000$ and $S/D_j = 1.5$) could lead the $\overline{Nu}_C$ values with $E/H = 0$ and 1/4 to the levels less than the smooth-walled counterparts. Further discussion on this issue will be addressed when the $\overline{Nu}_C$ data is examined.

As described previously, the stagnation point is horizontally shifted about 0.5 jet-diameter toward the dimple-centre due to the asymmetrical surface topology surrounding the jet-centre for the test result of $E/H = 1/4$ as shown in Fig. 6a. Also the stagnation heat transfer for $E/H = 1/4$ is further elevated from the smooth-walled and $E/H = 0$ conditions. There are heat transfer ripples developed in the inter-jet regions at the locations of $\pm 2X$ for condition of $E/H = 1/4$. These spots of $\pm 2X$ correspond to the geometric centres of each four surrounding dimples. With conditions of $E/H = 1/4$, the radial momentums of spent flows from each four surrounding stagnation points are not equilibrium due to the asymmetric topology for impinging jets. As a result, the additional flow momentum in radial direction is generated to assist the convection of spent fluids out of the inter-jet regions. Heat transfer ripples at the locations of $\pm 2X$ are therefore observed in Fig. 6a for test condition of $E/H = 1/4$. Further increase of E/H value from 1/4 to 1/2 resolves into another symmetrical topology condition for impinging jet-array. However, the jet-centre locates at the flat surface between convex dimples when $E/H = 1/2$. As shown in Fig. 6a for $E/H = 1/2$, the stagnation point coincides with the jet-centre and the Nu minimum develops between two adjacent jet-centres where corresponds to the apex of each dimple. Instead of having the heat transfer ripples developed at the inter-jet regions for $E/H = 1/4$

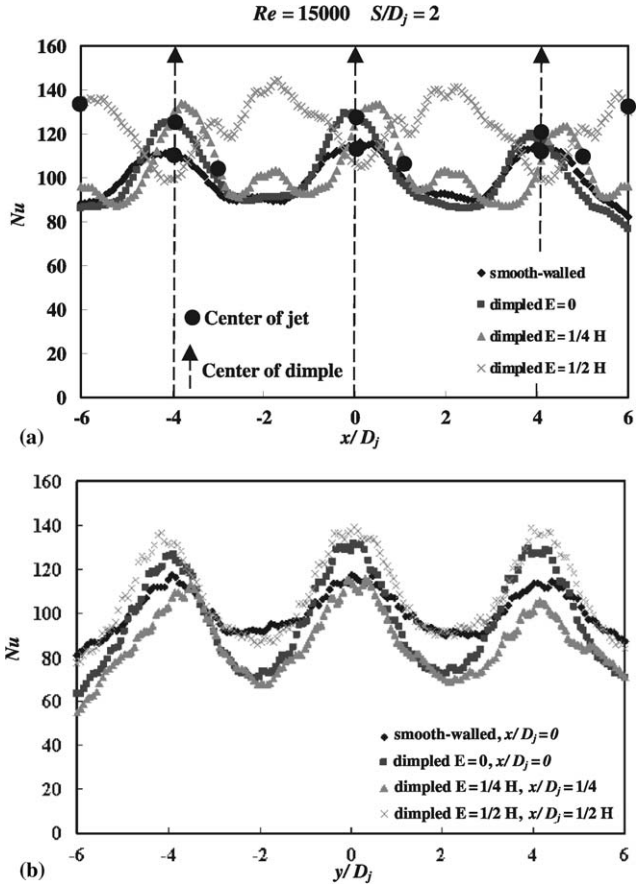

Fig. 6. Nusselt number distribution along the horizontal and vertical centre-lines with Reynolds number = 15,000 and $S/D_j = 2$ for the $E = 0$, $E = 1/4H$ and $E = 1/2H$.

condition, the heat transfer ripples consistently develop at the locations between jet-centre and dimple-centre for the test conditions with $E/H = 1/2$. Fig. 6b compares Nu profiles along Y axes that correspond to three vertical scanning-lines connecting three jet-centres for four test conditions. It is worth to mention that the stagnation heat transfers are not developed at the jet-centres for $E/H = 1/4$ condition. As shown in Fig. 6b, all the Nu profiles along the vertical scanning-lines follow the heat transfer pattern of impinging jet-array over smooth-walled surface irrespective to the eccentricity brought in the horizontal direction. Referring the smooth-walled data to as the comparison reference, heat transfers over convex-dimpled surface are impeded in the inter-jet regions but augmented over the stagnation regions. In view of the overall Nu levels for all the test results compared in Fig. 6a and b and for all the test results acquired from the present series of tests, the test conditions with $E/H = 1/2$ consistently provide the highest heat transfer rates relative to the results obtained from the smooth-walled, $E/H = 0$ and 1/4 conditions.

Fig. 7 examines the E/H impacts on heat transfer by plotting $Nu/Nu_{\text{smooth-wall}}$ ratios along $Y = 0$ axis and along three X axes of $X = 0$ ($E = 0$), $X = 1/4$ ($E = 1/4H$) and $X = 1/2$ ($E = 1/2H$) with $S/D_j = 1.5$, 2 and 4 at Reynolds number of 10,000. Due to the oval-shaped Nu contours developed over the dimpled surface as demonstrated in Fig. 5, the distributions of $Nu/Nu_{\text{smooth-wall}}$ ratio along X and Y axes perform differently. As shown in Fig. 7a–c, the $Nu/Nu_{\text{smooth-wall}}$ ratios along X axis for three eccentricities tested are higher than unity. The higher $Nu/Nu_{\text{smooth-wall}}$

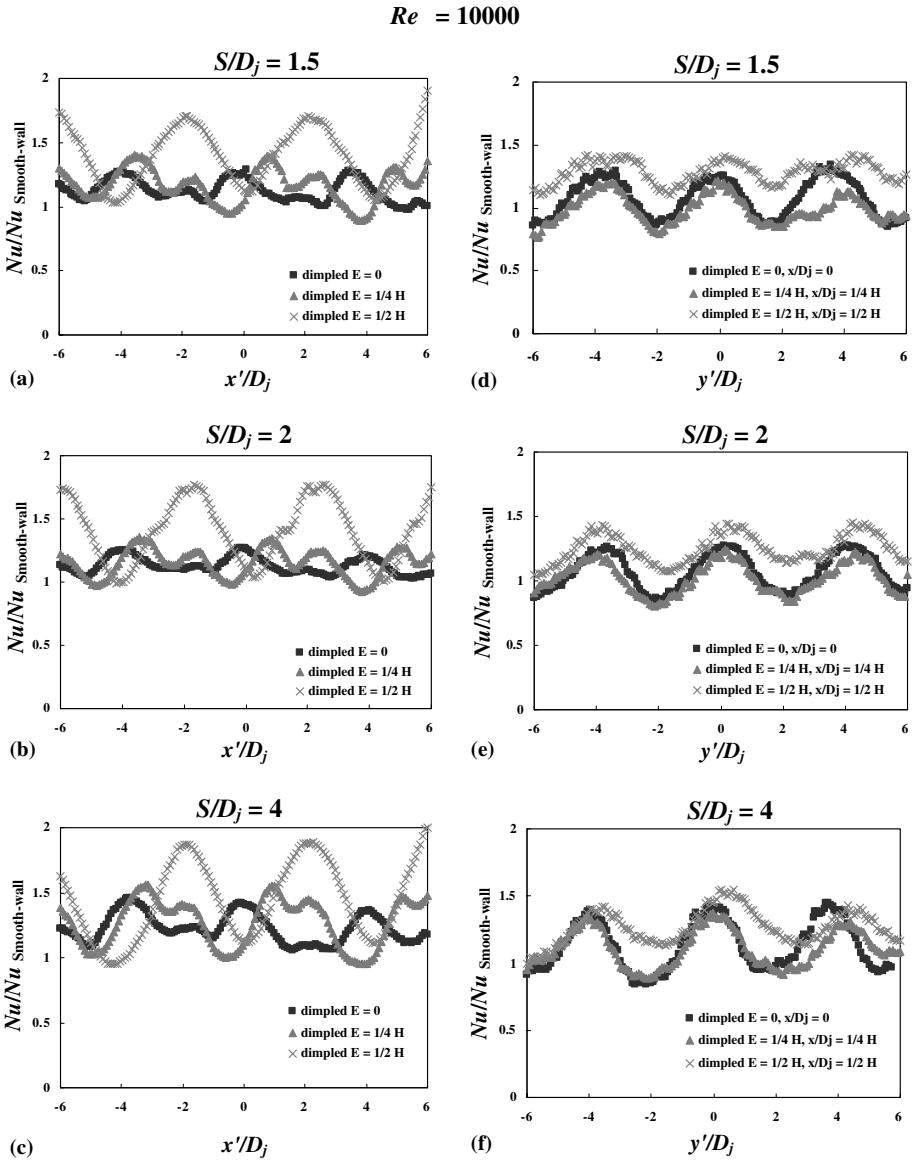

Fig. 7. Distributions of Nusselt number ratio along horizontal and vertical stagnation-lines at Reynolds number of 10,000 and $S/D_j = 1.5$, 2 and 4 for $E = 0$, $1/4H$ and $1/2H$.

ratios consistently develop at the stagnation points relative to those over the inter-jet regions. The X-wise heat transfer augmentations for $E/H = 1/2$ conditions are considerably higher than the counterparts with $E/H = 0$ and 1/4. For test conditions with $E/H = 1/4$, the X-wise profiles of $Nu/Nu_{\text{smooth-wall}}$ ratio follow the twin-ripple patterns due to the heat transfer humps developed at the middle locations between two adjacent dimple-centres. The $Nu/Nu_{\text{smooth-wall}}$ ratios are ranged from 1 to 2 as depicted in Fig. 7a–c. But the Y-wise variations of $Nu/Nu_{\text{smooth-wall}}$ ratio are in the range of 0.8–1.45 as shown in Fig. 7d–f, which are considerably less than the varying range detected along X axis. Thus the differences in $Nu/Nu_{\text{smooth-wall}}$ ratios along Y axis between three eccentricities tested are considerably suppressed from the X-wise levels. In particular, the Y-wise heat-transfer ratios for three E/H values tested are less than unity over the inter-jet regions. But the Y-wise $Nu/Nu_{\text{smooth-wall}}$ ratios in the stagnation regions are still above than unity. Nevertheless, as the jet centres are not corresponding to the stagnation points for the test conditions with $E/H =$ 1/4, the lowest $Nu/Nu_{\text{smooth-wall}}$ ratios consistently develop for the scenarios with $E/H = 1/4$ as indicated in Fig. 7d–f. Following the manner of data presentation shown in Fig. 7 but applied to different Reynolds numbers tested, it shows that the increase of Reynolds number reduces the heat transfer augmentation. In view of the S/D_j impacts for any fixed Reynolds number, the X-wise and Y-wise heat transfer enhancements systematically increase with the increase of S/D_j ratio as demonstrated in Fig. 7.

3.3. Spatially averaged heat transfer correlation over central jet region

The physics through which the variations of Re, S/D_j and E/H modify heat transfers involve the various modes of radial spent flows due to different impinging topologies for jet array and the modified inter-jet reactions. These flow mechanisms could be inter-correlated with the controlling parameters of Re, S/D_j and E/H. As a result, the spatially averaged Nusselt number over central jet region ($\overline{Nu}_C$) could be inter-correlated with the controlling parameters of Re, S/D_j and E/H. To unravel the functional relationship between Re, S/D_j and E/H for evaluating $\overline{Nu}_C$, the $\overline{Nu}_C$ data collected from each test condition with smooth-walled, $E/H = 0$, 1/4 or 1/2 at $S/D_j = 1.5$ and 8 is plotted against Re as shown in Fig. 8. If the limiting condition of vanishing forced convection is designated as $\overline{Nu}_C = 0$, the functional relationship between $\overline{Nu}_C$ and Re for each test condition, justified by the data trend revealed in Fig. 8, could be constructed as

$$\overline{Nu}_C = A\{S/D_j\} \times Re^{B\{S/D_j\}}. \quad (2)$$

The coefficient A and power index B of Eq. (2) are initially assumed to be functions of S/D_j for each test condition. Also compared in Fig. 8 are the $\overline{Nu}_C$ results evaluated from the empirical correlation proposed by Pan and Webb [14]

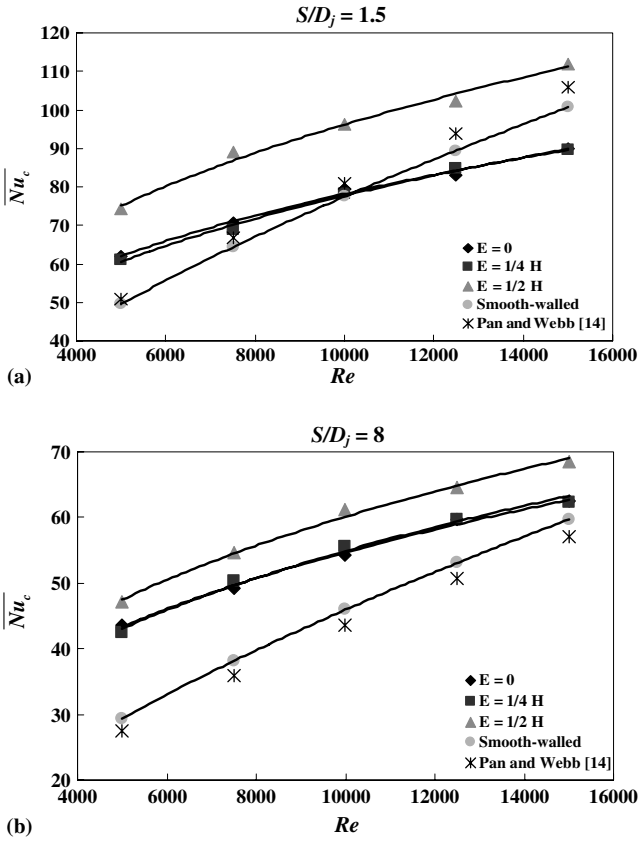

Fig. 8. Variation of $\overline{Nu}_C$ with jet Reynolds number for $E = 0$, $E = 1/4H$, $E = 1/2H$ at $S/D_j = 1.5$ and $S/D_j = 8$.

for the smooth-walled surface. As shown in Fig. 8, the present smooth-walled $\overline{Nu}_C$ values are in good agreements with the correlative results of Pan and Webb [14]. It is worth noting that, as indicated in Fig. 8a with $S/D_j = 1.5$, the smooth-walled $\overline{Nu}_C$ values are higher than those over the dimpled surfaces with $E/H = 0$ and 1/4 when Reynolds number is greater than 10,000. This particular result implies that the B values in Eq. (2) for test conditions of $E/H = 0$ and 1/4 are less than the smooth-walled B value. However, further increase of separation distance from 1.5 to $8D_j$ extends the effective Re range within which the $\overline{Nu}_C$ values over dimpled surface are higher than the smooth-walled counterparts. Therefore, the differences of A values between smooth-walled and dimpled-surface are increased when separation distance is increased. Nevertheless, for each option of $Re - S/D_j$ tested, the $\overline{Nu}_C$ values over dimpled surfaces with $E/H = 0$ and 1/4 are very close. The dimpled surface with $E/H = 1/2$ consistently provide the highest $\overline{Nu}_C$ values among the four tested scenarios.

The S/D_j impact on $\overline{Nu}_C$ for four test conditions is illustrated in Fig. 9 using the data obtained at Reynolds number of 10,000. The exponential decay of $\overline{Nu}_C$ against S/D_j is followed by four sets of test results. The data trends of $E/H = 0$ and 1/4 decay with the lower rates than the smooth-walled condition. The variation manners of $\overline{Nu}_C$ against S/D_j as revealed in Fig. 9 are repeated for all the Reynolds numbers tested. In order to develop a set of heat

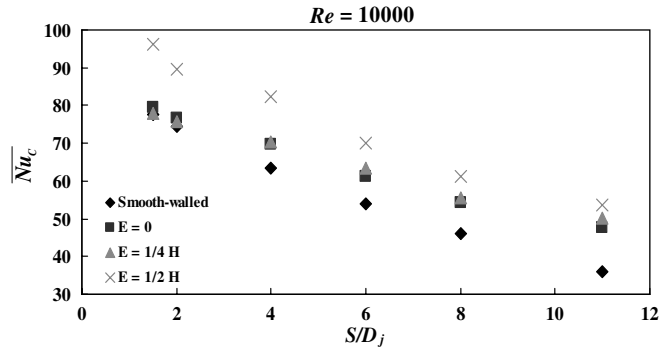

Fig. 9. Variation of Nu_C with S/D_j at Reynolds number of 10,000, for $E = 0$, $E = 1/4H$, and $E = 1/2H$.

transfer correlations for evaluating $\overline{Nu}_C$, each set of $\overline{Nu}_C$ data acquired from four test conditions is individually correlated using Eq. (2) as the functional structure. Fig. 10 depicts the varying trends of A and B coefficients against S/D_j. The B value, which quotes for the power index of Re in Eq. (2), tends to be invariant when S/D_j varies. The smooth-walled condition possesses the highest B value. When the eccentricity ratio increases from 0 to 1/2, a systematic increase of B value is obtained that implies the enhanced Re dependency for $\overline{Nu}_C$. Although the B value appears to be a very weak function of S/D_j for each set of test conditions, the exponential decay of $\overline{Nu}_C$ against S/D_j typified in Fig. 9 is recast by the varying manner of coefficient A as shown in Fig. 10a. Justified by the regression-type evidence depicted in Fig. 10, the heat transfer correlations for evaluating $\overline{Nu}_C$ are obtained as

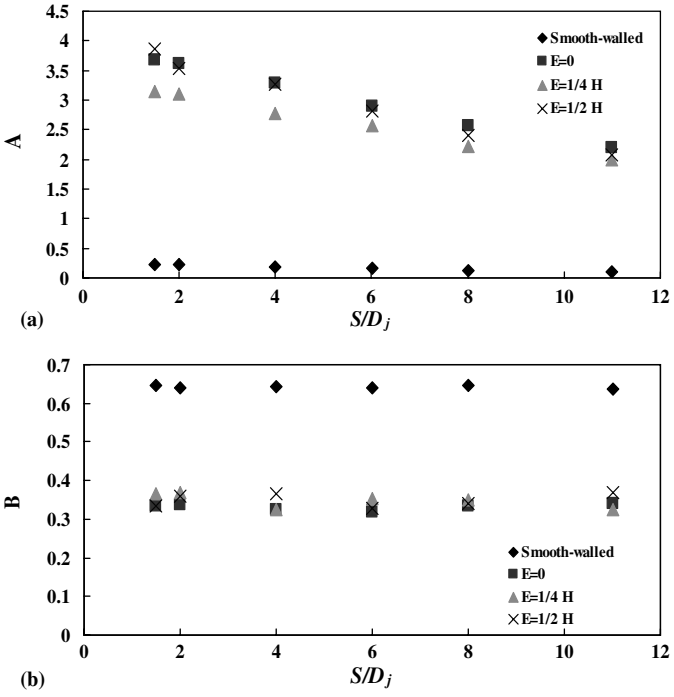

Fig. 10. Variation of coefficients A and B with S/D_j for smooth-walled, $E = 0$, $E = 1/4H$, and $E = 1/2H$.

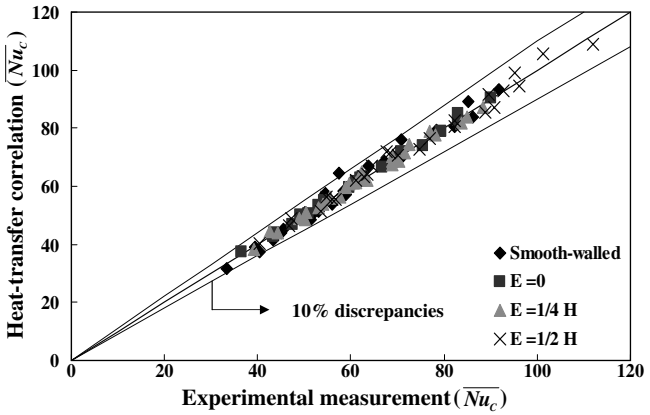

Fig. 11. Comparison of experimental data with heat transfer correlation.

$$\overline{Nu}_C = 0.228\,e^{-0.08S/D_j} \times Re^{0.646} \quad \text{(smooth-walled surface)}, \tag{3}$$

$$\overline{Nu}_C = 4.028\,e^{-0.055S/D_j} \times Re^{0.332} \quad \text{(dimpled surface with } E/H = 0), \tag{4}$$

$$\overline{Nu}_C = 3.393\,e^{-0.049S/D_j} \times Re^{0.348} \quad \text{(dimpled surface with } E/H = 1/4), \tag{5}$$

$$\overline{Nu}_C = 4.148\,e^{-0.065S/D_j} \times Re^{0.35} \quad \text{(dimpled surface with } E/H = 1/2). \tag{6}$$

The overall success of the proposed correlations embodied in Eqs. (3)–(6) for $\overline{Nu}_C$ over the smooth-walled and dimpled impinging surfaces is examined by comparing all the experimental measurements with the empirical predictions as indicated in Fig. 11. As shown in Fig. 11, the values of $\overline{Nu}_C$ indicating by the ranges of data spreads with test condition of $E/H = 1/2$ are generally higher. The maximum discrepancy of $\pm 10\%$ between the experimental and correlative results is achieved for the entire set of data. Even with the presence of surface-dimple complexities for the jet array, the experimentally based correlations could still provide the reasonable evaluations for spatially averaged heat transfers over central jet region.

4. Conclusions

The detailed heat transfer measurements of impinging jet-array over smooth-walled and convex-dimpled surfaces are performed to study the combined effects of Re, S/D_j and E/H on heat transfer. The heat transfer physics are inter-correlated with the controlling parameters of Re, S/D_j and E/H. Several salient points that have been identified are as follows:

1. With adequate selection of Re and S/D_j, the moderated jet-to-jet interference and shrinkage of inter-jet region along with elevated heat transfers over stagnation regions assist to augment heat transfer with improved uniformity over the convex-dimpled surface. Further increase of Re or/and decrease of S/D_j moderate the

improvement of heat transfer performance attributed from the surface dimples. For test conditions of $Re \geqslant 10{,}000$ and $S/D_j = 1.5$, Nu levels in the inter-jet regions over convex-dimpled surface with $E/H = 0$ and 1/4 are less than the smooth-walled counterparts so that the $\overline{Nu}_C$ values for $E/H = 0$ and 1/4 are less than the smooth-walled levels.

2. The isolated Re and S/D_j impacts on $\overline{Nu}_C$ are, respectively, indexed by A and B coefficients in Eq. (2). A systematic increase of E/H ratio results in the corresponding increase of B value that reflects the enhanced dependency of $\overline{Nu}_C$ on Re. The exponential decay of $\overline{Nu}_C$ with increased S/D_j is confirmed fro all the test scenarios which is recast by $A\{S/D_j\}$ function. As coefficients A and B both vary with E/H ratio, the uncoupling effects of Re and S/D_j on $\overline{Nu}_C$ are intercorrelated with E/H.
3. The symmetrical and asymmetrical surface topologies for impinging jet-array are, respectively, generated for test conditions with $E/H = 0$, 1/2 and 1/4. Due to the asymmetrical surface topology surrounding the jet-centre for test conditions of $E/H = 1/4$, each jet issued from orifice plat is bend toward the dimple-centre so that its stagnation point is horizontally shifted about 0.5 jet-diameter toward the dimple centre. Among each four comparable sets of test scenarios, the highest $\overline{Nu}_C$ levels consistently develop over the dimpled surface for the test conditions with $E/H = 1/2$; while the $\overline{Nu}_C$ values for test conditions of $E/H = 0$ and 1/4 are in close agreements.
4. In conformity with the experimental evidences, a regression-type analysis is performed to generate the empirical heat transfer correlations that permit the evaluations of $\overline{Nu}_C$ values over the smooth-walled and the convex-dimpled surfaces with $E/H = 0$, 1/4 and 1/2.

References

[1] R. Viskanta, Heat transfer to impinging isothermal gas and flame jets, Exp. Thermal Fluid Sci. 6 (1993) 111–134.

[2] C.J. Hoogendoorn, The effect of turbulence on heat transfer at a stagnation point, Int. J. Heat Mass Transfer 20 (1977) 1333–1338.

[3] R.J. Goldstein, W.S. Seoul, Heat transfer to a row of impinging circular air jets including the effect of entrainment, Int. J. Heat Mass Transfer 34 (1991) 2133–2147.

[4] L. Huang, M.S. El-Genk, Heat transfer and flow visualization experiments of swirling, multi-channel, and conventional impinging jets, Int. J. Heat Mass Transfer 41 (3) (1998) 583–600.

[5] S.C. Arjocu, J.A. Liburdy, Identification of dominant heat transfer modes associated with the impingement of an elliptical jet array, ASME J. Heat Transfer 122 (2000) 240–247.

[6] L.M. Su, S.W. Chang, Detailed hest transfer measurements of impinging jet arrays issued from grooved surface, Int. J. Thermal Sci. 41 (2002) 823–841.

[7] E.M. Sparrow, B.J. Lovell, Heat transfer characteristics of an obliquely impinging circular jet, ASME J. Heat Transfer 102 (1980) 202–209.

[8] P. Hrycak, Heat transfer from a row of impinging jets to concave cylindrical surfaces, Int. J. Heat Mass Transfer 24 (1981) 407–418.

[9] C. Gau, I.C. Lee, Flow and impinging cooling heat transfer along triangular rib-roughened walls, Int. J. Heat Mass Transfer 43 (2000) 4405–4418.

[10] E.E.M. Olsson, L.M. Ahrne, A.C. Trägårdh, Heat transfer from a slot air jet impinging on a circular cylinder, J. Food Eng. 63 (2004) 393–401.

[11] R.N. Koopman, E.M. Sparrow, Local and average transfer coefficients due to an impinging rows of jets, Int. J. Heat Mass Transfer 19 (1976) 673–683.

[12] B.R. Hollworth, L. Dagan, Arrays of impinging jets with spent fluid removal through vent holes on the target surface – Part I: Average heat transfer, ASME J. Eng. Power 102 (1980) 994–999.

[13] A.I. Behbahani, R.J. Goldstein, Local heat transfer to staggered arrays of impinging circular air jets, ASME J. Eng. Power 105 (1983) 354–360.

[14] Y. Pan, B.W. Webb, Heat transfer characteristics of arrays of free-surface liquid jets, ASME J. Heat Transfer 117 (1995) 878–883.

[15] L.B.Y. Aldabbagh, I. Sezai, Numerical simulation of three-dimensional laminar multiple impinging square jets, Int. J. Heat Fluid Flow 23 (2002) 509–518.

[16] P. Brevet, C. Dejeu, E. Dorignac, M. Jolly, J.J. Vullierme, Heat transfer to a row of impinging jets in consideration of optimization, Int. J. Heat Mass Transfer 25 (2002) 4191–4200.

[17] L.B.Y. Aldabbagh, I. Sezai, Three-dimensional numerical simulation of an array of impinging laminar square jets with spent fluid removal, Int. J. Thermal Sci. 43 (2004) 241–247.

[18] A.M. Huber, R. Viskanta, Effect of jet-to-jet spacing on convective heat transfer to confined, impinging arrays of axisymmetric air jets, Int. J. Heat Mass Transfer 37 (18) (1994) 2859–2869.

[19] D.E. Metzger, R.J. Korstad, Effects of crossflow on impingement heat transfer, ASME J. Eng. Power 94 (1972) 35–42.

[20] L.W. Florschuetz, R.A. Berry, D.E. Metzger, Periodic streamwise variation of heat transfer coefficients for inline and staggered arrays of circular jets with crossflow of spent air, ASME J. Heat Transfer 102 (1) (1980) 132–137.

[21] L.W. Florschuetz, C.R. Truman, D.E. Metzger, Streamwise flow and heat transfer distribution for jet impingement with crossflow, ASME J. Heat Transfer 103 (2) (1981) 337–342.

[22] L.W. Florschuetz, D.E. Metzger, C.C. Su, Y. Isoda, H.H. Tseng, Heat transfer characteristics for jet array impingement with initial crossflow, ASME J. Heat Transfer 106 (1) (1984) 34–41.

[23] N. Obot, T.A. Trabold, Impingement heat transfer within arrays of circular jets. Part I: Effects of minimum, intermediate, and complete crossflow for small and large spacings, ASME J. Heat Transfer 109 (4) (1987) 872–879.

[24] A.M. Huber, R. Viskanta, Convective heat transfer to a confined impinging array of air jets with spent air exits, ASME J. Heat Transfer 116 (1994) 570–576.

[25] Y. Huang, S.V. Ekkad, J.C. Han, Detailed heat transfer distributions under an array of orthogonal impinging jets, J. Thermophys. Heat Transfer 12 (1) (1998) 73–79.

[26] K. Garrett, B.W. Webb, The effect of drainage configuration on heat transfer under an impinging liquid jet array, ASME J. Heat Transfer 121 (1999) 803–810.

[27] H.S. Sheriff, D.A. Zumbrunnen, Local and instantaneous heat transfer characteristics of arrays of pulsating jets, ASME J. Heat Transfer 121 (1999) 341–348.

[28] D.K. Lee, K. Vafai, Comparative analysis of jet impingement and microchannel cooling for high heat flux application, Int. J. Heat Mass Transfer 42 (1999) 1555–1568.

[29] H. Martin, Heat and mass transfer between impinging gas jets and solid surfaces, Adv. Heat Transfer 8 (1977) 1–60.

[30] R. Gardon, J.C. Akfirat, Heat transfer characteristics of impinging two-dimensional air jets, ASME J. Heat Transfer 88 (1966) 101–108.

[31] M. Korger, F. Krizek, Mass transfer coefficient in impingement flow from slotted nozzles, Int. J. Heat Mass Transfer 9 (1966) 337–344.

[32] S. Parneix, M. Behnia, P.A. Durbin, Prediction of turbulent heat transfer in an axisymmetric jet impinging on a heated pedestal, ASME J. Heat Transfer 121 (1999) 43–49.
[33] Y. Kondo, H. Matsushima, T. Komatsu, Optimization of pin-fin Heat sink for impingement cooling in electronic packaging, ASME J. Electron. Packag. 122 (2000) 240–246.
[34] C. Gau, C.C. Lee, Impingement cooling flow structure and heat transfer along rib-roughened walls, Int. J. Heat Mass Transfer 35 (1992) 3009–3020.
[35] C. Gau, I.C. Lee, Flow and impingement cooling heat transfer along triangular rib-roughened walls, Int. J. Heat Mass Transfer 43 (2000) 4405–4418.
[36] S.W. Chang, L.M. Su, Y. Zheng, Reciprocating impingement jet heat transfer with surface rib, J. Exp. Heat Transfer 13 (2000) 275–297.
[37] S. Polat, B. Huang, A.S. Mujumbar, W.J.M. Douglas, Numerical flow and heat transfer under impinging jets: a review, in: C.L. Tien (Ed.), Annual Review of Numerical Fluid Mechanics and Heat Transfer, vol. 2, Hemisphere, Washington, DC, 1989, pp. 157–197.
[38] Editorial Board of ASME Journal of Heat Transfer, Journal of Heat Transfer policy on reporting uncertainties in experimental measurements and results, ASME J. Heat Transfer 115 (1993) 5–6.